



CrossMark  
click for updates

Cite this: *RSC Adv.*, 2016, 6, 26535

Received 13th January 2016  
Accepted 3rd March 2016

DOI: 10.1039/c6ra01091a

[www.rsc.org/advances](http://www.rsc.org/advances)

# Porous $\beta$ -MnO<sub>2</sub> nanoplates derived from MnCO<sub>3</sub> nanoplates as highly efficient electrocatalysts toward oxygen evolution reaction†

Jun Kim,<sup>‡,ab</sup> Ju Seong Kim,<sup>‡,c</sup> Hionsuck Baik,<sup>d</sup> Kisuk Kang<sup>\*c</sup> and Kwangyeol Lee<sup>\*ab</sup>

$\beta$ -MnO<sub>2</sub> has not been considered as an effective catalyst toward the oxygen evolution reaction due to its lack of active di- $\mu_2$ -oxo bridged Mn centres and inaccessibility to the inner Mn atoms. We have envisioned that  $\beta$ -MnO<sub>2</sub> can be made catalytically active by making the inner Mn atoms accessible. In order to accomplish this, we have synthesized MnCO<sub>3</sub> nanoplates *via* a solution route and converted them into highly porous  $\beta$ -MnO<sub>2</sub> nanoplates with very high surface area. In addition to the reduced overpotential of 450 mV at 10 mA cm<sup>-2</sup>, the derived Tafel slope was 78.2 mV dec<sup>-1</sup>, showing a superior catalytic activity of the porous nanoplate, which is comparable to the catalytic performance of best performing  $\alpha$ -MnO<sub>2</sub> phase. The importance of surface-bound catalytic Mn sites in highly porous  $\beta$ -MnO<sub>2</sub> nanoplates is also demonstrated by Au loading-induced blockage of them and corresponding catalytic activity deterioration.

Dwindling natural energy resources and environmental issues associated with their usage call for urgent developments in economical and clean energy technologies.<sup>1–3</sup> Hydrogen is considered as a clean future energy source, and therefore an efficient water splitting process for hydrogen production is in great demand.<sup>1–3</sup> Water oxidation, or oxygen evolution reaction (OER), is one of the major hurdles to an efficient water splitting reaction, because it is energetically unfavourable in nature.<sup>4</sup> Consequently, considerable efforts have been put into the development of efficient OER catalysts. Metal oxides of precious metals such as RuO<sub>2</sub> and IrO<sub>2</sub> have shown high catalytic

activities toward OER.<sup>5,6</sup> Practical applications of them, however, have not been realized due to the high cost in the catalyst production.<sup>7–9</sup> Inexpensive first-row transition metal oxides, therefore, are being intensively studied for the potential applications as OER catalysts.<sup>10–13</sup> Manganese oxides, in particular, are of a great interest due to their wide range of oxidation states and possible crystal structures.<sup>9,14</sup>  $\alpha$ -MnO<sub>2</sub> is well-known for its excellent catalytic activity owing to its large 2 × 2 internal channels providing numerous passages for ions and other molecules,<sup>15</sup> and this feature, in addition to the catalytically active surface, allows the internal portion under the surface to be used as an active material. On the other hand,  $\beta$ -MnO<sub>2</sub> is generally considered to be catalytically inferior due to its unique connectivity of MnO<sub>6</sub> octahedrons, which results in only a small number of catalytically active sites.<sup>16</sup> In addition, the internal portion of  $\beta$ -MnO<sub>2</sub> could not be utilized for catalytic purpose, because very narrow 1 × 1 internal channels prohibit the passage of small chemical species.<sup>17</sup> These inherent structural disadvantages of  $\beta$ -MnO<sub>2</sub> in catalytic applications might be overcome by making the  $\beta$ -MnO<sub>2</sub> highly porous; porous  $\beta$ -MnO<sub>2</sub> might allow access of small chemical species to the catalytically active sites which were previously inaccessible. Introduction of porosity to  $\beta$ -MnO<sub>2</sub>, however, poses a formidable challenge.

In principle, porous  $\beta$ -MnO<sub>2</sub> structure can be prepared if a low density nanocrystalline precursor is abruptly converted to  $\beta$ -MnO<sub>2</sub> phase. MnO<sub>2</sub> nanostructures can be prepared from MnCO<sub>3</sub> by calcination.<sup>18</sup> With MnCO<sub>3</sub> nanoparticles with a suitable structural feature to enable a fast CO<sub>2</sub> release, it should be feasible to form highly porous manganese oxide nanomaterials. In this work, we report a facile synthetic route to single crystalline MnCO<sub>3</sub> nanoplates (MCP) and their transformation to highly porous  $\beta$ -MnO<sub>2</sub> nanoplates (PMOP) *via* calcination as shown in Scheme 1. Thus prepared PMOP exhibits a superior catalytic activity toward OER.

In a typical synthesis of MCP, a slurry of Mn(OAc)<sub>2</sub> (2.50 mmol), sodium oleate (NaOA, 2.50 mmol), and oleylamine (5.00 mmol) was prepared in a 100 mL Schlenk tube equipped with a bubbler. The tube containing the slurry was evacuated for 10

<sup>a</sup>Center for Molecular Spectroscopy and Dynamics, Institute for Basic Science (IBS), Seoul 02841, Korea

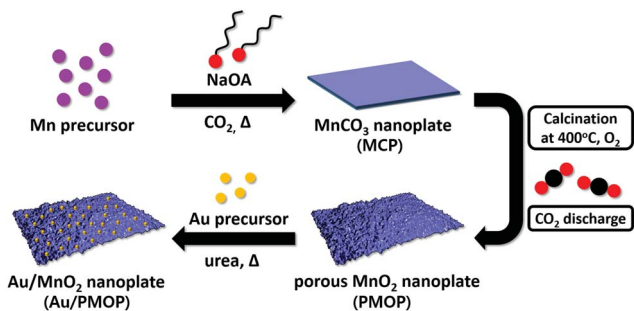
<sup>b</sup>Department of Chemistry and Research Institute for Natural Sciences, Korea University, Seoul 02841, Republic of Korea. E-mail: kylee@korea.ac.kr

<sup>c</sup>Department of Materials Science and Engineering, Research Institute of Advanced Materials, Seoul National University, 599 Gwanak-ro, Gwanak-gu, Seoul 08826, Republic of Korea. E-mail: matlgen1@snu.ac.kr

<sup>d</sup>Korea Basic Science Institute (KBSI), Seoul 02841, Korea

† Electronic supplementary information (ESI) available. See DOI: 10.1039/c6ra01091a

‡ These authors contributed equally.



Scheme 1 Synthetic routes to porous MnO<sub>2</sub> nanoplate and Au deposition.

min at room temperature, and then the reaction mixture was maintained at 290 °C under CO<sub>2</sub> flow with magnetic stirring for 1 h. The precipitated white product was washed with copious amount of hexane, ethanol and water to remove any excess reagents. Finally, the white precipitate was treated with dilute acetic acid (5% v/v) for 30 min to remove surface bound surfactants, and washed several times with ethanol. The final product was dried in an oven at 45 °C. The X-ray diffraction (XRD) pattern of as-synthesized MCP indicates hexagonal close packing system with  $R\bar{3}c$  space group (JCPDS #01-086-0172. See Fig. S1†). As shown in the transmission electron microscope (TEM) images in Fig. 1a and b, MCP exhibits a flat rhombohedral morphology; the width of the nanoplates ranges from 100 nm to 200 nm and the average thickness is measured to be  $13.1 \pm 3.4$  nm. Fig. 1d shows a highly magnified side-view of MCP, and the high-resolution transmission electron microscope (HRTEM) image and fast Fourier transformation (FFT) analysis

of them reveal that nanoplates are single-crystalline with the wide top and bottom faces of the nanoplates being {012} facets.

The formation of MnCO<sub>3</sub> phase and the nanoplate morphology are critically dependent on the presence of both NaOA and CO<sub>2</sub>. In the absence of either NaOA or CO<sub>2</sub>, MnO phase, instead of MnCO<sub>3</sub>, was produced from the decomposition of Mn(OAc)<sub>2</sub> (Table S1†). Obviously, the MnCO<sub>3</sub> phase is stabilized in the presence of CO<sub>2</sub>, which shifts the chemical reaction equilibrium from MnO to MnCO<sub>3</sub>. The basic nature of NaOA might have contributed to the stability of MnCO<sub>3</sub> phase, which can be easily destabilized in an acidic condition. NaOA seems to act as a structure directing agent as well, because the thickness of the nanoplate can be controlled by varying the amount of NaOA. (Fig. S2†) The thickness of the nanoplate gradually decreases as the amount NaOA is increased, which may indicate that NaOA prefers {012} facets of MnCO<sub>3</sub> crystal, stabilizing {012} facets and preventing the growth along the [012] zone axis.

When other Mn precursors with oxygen-containing ligands such as formate, nitrate, or acetylacetonate were used, the formation of MnCO<sub>3</sub> phase was also observed. On the other hand, the decomposition of MnCl<sub>2</sub> in the presence of NaOA and CO<sub>2</sub> produced only MnO phase. Interestingly, the addition of sodium acetate to the latter reaction mixture led to the formation of plate-like MnCO<sub>3</sub> nanostructures, indicating the role of acetate ligands in both stabilizing the MnCO<sub>3</sub> phase and forming the nanoplate morphology. Nanoplate morphology, however, could not be obtained from decomposition of Mn precursors with formate, nitrate, or acetylacetonate ligands, even when sodium acetate was added to the reaction mixture. The acetate species might not compete effectively with these

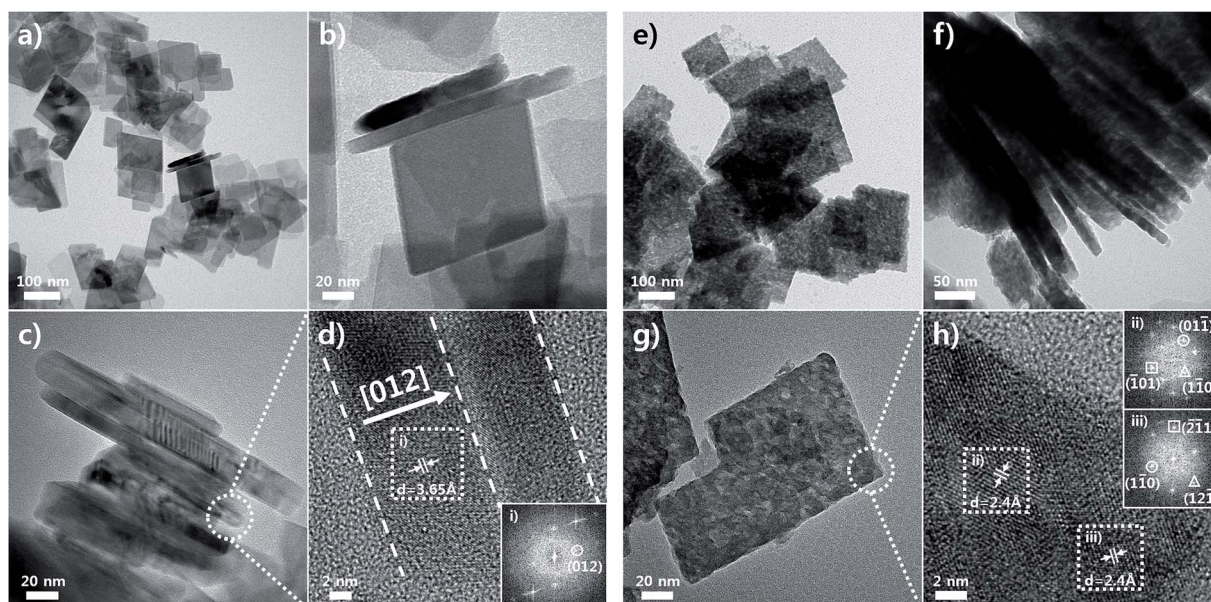


Fig. 1 Structural analysis of MnCO<sub>3</sub> nanoplate (MCP) and porous  $\beta$ -MnO<sub>2</sub> nanoplate (PMOP). (a and b) TEM images of MCP and (c) side-view of stacked nanoplates. (d) HRTEM image of stacked MCP showing that the wide top and bottom faces of a nanoplate has {012} facets; the FFT pattern of the area enclosed by a dotted rectangle is shown in (i). (e) TEM images of PMOP and (f) side-view of stacked PMOP. (g) TEM image showing the rough topography of PMOP surface. (h) HRTEM image of PMOP showing different zone axes of [111] and [113] with corresponding (ii) and (iii) FFT patterns, respectively.

oxygen-containing ligands for binding to Mn centres to give the nanoplate morphology.

MCP can be converted into PMOP through calcination (Scheme 1). Thermogravimetric analysis (Fig. S5†) of MCP under O<sub>2</sub> reveals that the conversion into MnO<sub>2</sub> begins around 400 °C, which is accompanied by a drastic decrease in weight due to the rapid discharge of CO<sub>2</sub>. The TEM image of PMOP in Fig. 1e and f show that the original plate morphology remains mostly intact and the surface of PMOP is very rough due to a rapid CO<sub>2</sub> discharge at high temperature. The XRD pattern of the resulting PMOP shows very broad peaks (Fig. S6†), suggesting very small grain sizes. The HRTEM analysis in Fig. 1h shows that PMOP consists of many nanosized single crystalline domains whose zone axes are randomly distributed. In addition, owing to the high porosity and rough surface (Fig. 1f and g), PMOP shows a very high Brunauer–Emmett–Teller (BET) surface area of 96.7 m<sup>2</sup> g<sup>-1</sup> and pore volume of 0.77 cm<sup>3</sup> g<sup>-1</sup> (Fig. S7†).

Hetero-metal doping or deposition has been previously employed to enhance the water oxidation ability of metal oxide catalysts.<sup>19–21</sup> Au deposition *via* various chemical and physical methods has been reported to enhance the catalytic activity of manganese oxide nanomaterials.<sup>22–24</sup> In our study, three Au-deposited samples, namely, low Au/PMOP (L-Au/PMOP), medium Au/PMOP (M-Au/PMOP) and high Au/PMOP (H-Au/PMOP), were obtained *via* urea-assisted formation of Au nanoparticles and their deposition. The Au nanoparticle coverage in these samples and the oxidation states of constituting atoms were analysed by TEM, HRTEM and X-ray photoelectron spectroscopy (XPS) (Fig. S8 and S9†). The TEM and HRTEM images of H-Au/PMOP are shown in Fig. 2 as an example, and Au nanoparticles with an average size of 2.54 nm are uniformly distributed on PMOP and, in addition, line profile analysis was performed to further confirm the presence of Au nanoparticles. (Fig. S10†) On the contrary, Au nanoparticles are barely observed for L-Au/PMOP. Before Au deposition, the Mn valence state of the as-synthesized PMOP was measured to be 3.84 by XPS analysis, which may indicate the presence of Mn vacancies in MnO<sub>2</sub> lattices.<sup>25</sup> As presented in Table 1, the Mn valence state gradually decreases as the deposition of Au increases. Chen's group reported a similar result with Au doped MnO<sub>2</sub> film, and the oxidation state of Mn decreases because of the gain of electrons from Au, consistent with the first principle calculation and XPS measurements.<sup>26</sup>

Catalytic activities of PMOP, L-Au/PMOP, M-Au/PMOP and H-Au/PMOP nanoplates toward OER were investigated by cyclic voltammetry (CV) in 1 M KOH aqueous solution. Prepared catalysts were deposited on carbon paper by drop-casting method with a loading amount of 0.4 mg cm<sup>-2</sup>. The OER activity of 20 wt% Ir/C (Premetek) was also measured to compare with those of our catalysts. The OER activity curves were obtained by averaging the forward and the reverse curves for capacitive current. As shown in Fig. 3a, PMOP exhibited an onset potential of water oxidation at an overpotential of 300 mV and a low overpotential of 450 mV at a current density of 10 mA cm<sup>-2</sup>. The Tafel slope of PMOP was measured to be 78.2 mV dec<sup>-1</sup>. It is notable that the OER activity of PMOP matches that

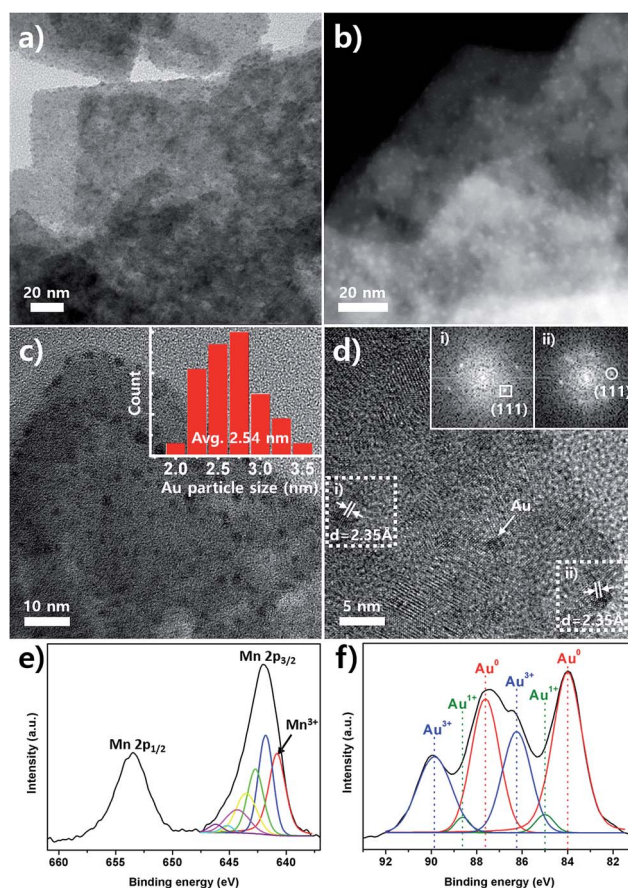


Fig. 2 Structural analysis of Au deposited PMOP (H-Au/PMOP). (a) TEM image and (b) STEM image of H-Au/PMOP showing a uniform coverage of Au nanoparticles. (c and d) HRTEM images showing Au nanoparticles with 0.235 nm *d*-spacing which corresponds to {111} crystal planes of Au. The FFT patterns are shown in (i) and (ii). Deconvoluted XPS spectra of (e) Mn 2p and (f) Au 4f of H-Au/PMOP.

Table 1 Changes in valence states of Mn and Au depending on Au deposition

Catalyst	Mn valence state <sup>a</sup>	Au valence state <sup>a</sup>	Au atomic % by ICP-AES
PMOP	3.84	—	—
L-Au/PMOP	3.78	—	2.6
M-Au/PMOP	3.75	0.71	4.6
H-Au/PMOP	3.72	1.05	6.0

<sup>a</sup> Valence states are calculated by deconvoluting the XPS spectra of each sample.

of the commercial Ir/C which has an overpotential of 350 mV at 10 mA cm<sup>-2</sup> and Tafel slope of 76.7 mV dec<sup>-1</sup>. The superior catalytic activity of PMOP may be attributed to the highly porous nature which can provide reactant molecules high surface area and numerous passages to catalytically active sites. Suib's group recently reported the structure–property relationship of MnO<sub>2</sub> as well as a summary of OER catalytic activities of nano-structured MnO<sub>2</sub> with various crystal structures.<sup>27</sup> Notably, the

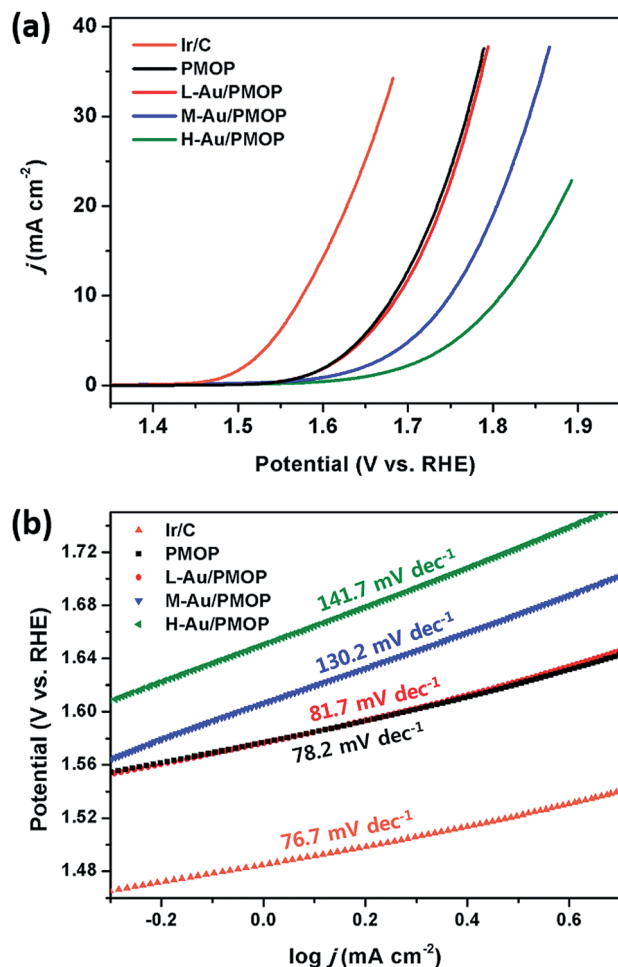


Fig. 3 Electrochemical water oxidation measurements of Ir/C (20 wt%), PMOP, L-Au/PMOP, M-Au/PMOP and H-Au/PMOP. (a) Capacitive background corrected polarization curves in 1 M KOH electrolyte. (b) The corresponding Tafel plots.

catalytic performance of PMOP of our study is comparable to that of the best performing  $\alpha$ -MnO<sub>2</sub> catalysts and better than the recently reported screen-printed  $\beta$ -MnO<sub>2</sub> film.<sup>27,28</sup> Although the overpotential of PMOP is higher than that of the commercial Ir/C, PMOP has the lowest overpotential without any conductive support compared to those of the MnO<sub>2</sub> catalysts reported to date. We believe that the low overpotential of PMOP results from the increased contact surface with the electrode and the short travelling distance for electrons owing to its thin plate morphology. While PMOP showed excellent catalytic performance, interestingly against our expectations, the OER activities of the three Au-deposited samples deteriorated with increasing Au loading contents as can be seen in Fig. 3. The overpotentials of L-Au/PMOP, M-Au/PMOP and H-Au/PMOP were 460, 520 and 580 mV, respectively, at a current density of 10 mA cm<sup>-2</sup> and the Tafel slopes of these Au-deposited PMOP increased to 81.7, 130.2 and 141.7 mV dec<sup>-1</sup>, respectively, as shown in Fig. 3b. Furthermore, the chronopotentiometry of PMOP and Au-deposited PMOP shows that bare PMOP exhibits the best stability among the MnO<sub>2</sub> catalysts in our study (Fig. S11†).

Recent studies have suggested that the catalytic activity for OER originates from the nature of the bonding between metal centres and oxygen and that the presence of di- $\mu_2$ -oxo bridged metal ions is a common feature in other transition metal oxide catalysts for water oxidation.<sup>29–31</sup>  $\beta$ -MnO<sub>2</sub> prevalently possesses mono- $\mu_2$ -oxo bridged Mn ions because its crystal structure is derived from corner-shared MnO<sub>6</sub> octahedrons, resulting in inferior catalytic activity as compared to those of other MnO<sub>2</sub> polymorphs.<sup>25,27</sup> Moreover, the internal Mn ions, due to narrow inner channels, are not easily accessible for reactant molecules. However, the porosity of the  $\beta$ -MnO<sub>2</sub> nanostructure of this study might have provided numerous pathways to previously inaccessible internal Mn ions on  $\beta$ -MnO<sub>2</sub> {110} with di- $\mu_2$ -oxo bridged Mn centres.<sup>25,32</sup> Furthermore, the 2D nanoplate morphology, while shortening the travelling distance for reactant molecules, decreases the number of inaccessible Mn ions by reducing the internal volume and increasing the surface confined atoms at the same time. In short, the increased number of accessible di- $\mu_2$ -oxo bridged Mn ions in the porous MnO<sub>2</sub> nanoplate, due to the synergy between the porosity and nanoplate morphology, might have led to the excellent catalytic performance of  $\beta$ -MnO<sub>2</sub> nanoplate of this study. Another contributing factor to the enhanced catalytic performance might be the presence of defect sites such as Mn vacancies.<sup>33</sup> When MnCO<sub>3</sub> is converted to  $\beta$ -MnO<sub>2</sub> *via* calcination, the conversion of crystal phase must occur from hexagonal close packing (hcp) system to a completely different phase of face-centered tetragonal (fct) system. This drastic change in crystal structures might result in the formation of very small, numerous grains of MnO<sub>2</sub> nanocrystals with a large number of Mn vacancies. These vacancies might help di- $\mu_2$ -oxo bridged Mn ions become more predominant than di- $\mu_3$ -oxo bridged Mn ions, thus providing a higher number of active sites for water coordination.<sup>25</sup> Also, uncoordinated oxygen atoms due to Mn vacancies can provide proton binding sites;<sup>34</sup> Dau's group proposed that the resulting  $\mu$ -OH units may facilitate proton-coupled electron transfer (PCET), which is considered a critical factor in water oxidation.<sup>16</sup> Since the defect sites are coordinatively unsaturated with many dangling bonds, the nucleation and growth of Au nanoparticle occurring on those defect sites can lead to the significant passivation of OER active sites. The deteriorating catalytic performance of PMOP with increased Au contents indicates that the blockage of catalytically active sites is very severe with Au-deposition. The enhanced catalytic activity with Au-loading of catalytic metal oxides, observed in other reported studies, could not be repeated in our study.

We also investigated the catalytic performance of PMOP toward oxygen reduction reaction (ORR) (Fig. S12†). According to the half-wave potentials in the ORR curves of the porous  $\beta$ -MnO<sub>2</sub> nanoplates (0.647 V) and 20 wt% Pt/C (0.918 V), the MnO<sub>2</sub> sample shows much inferior catalytic property to that of Pt/C sample. However, the ORR performance of PMOP in this study, with a slightly lower half-wave potential, is similar to that of the oxygen-deficient  $\beta$ -MnO<sub>2</sub> reported by Cheng *et al.*<sup>35</sup>

## Conclusion

In conclusion, we have synthesized PMOP with a very high surface area *via* calcination of highly crystalline MCP and demonstrated their excellent catalytic activity toward OER. The number density of catalytically active Mn sites in PMOP is greatly increased due to their unique morphological features such as 2D morphology and porosity. In addition, numerous Mn vacancies in PMOP, generated from abrupt material transformation, might have further contributed to the enhanced catalytic performance. The important role of surface bound catalytic sites is demonstrated by the deteriorated catalytic activity with increased Au-loading on the surface. We believe that the synthetic methodology of this study might be applicable to the preparation of other catalytically useful metal oxide nanostructures. It is quite intriguing to study the catalytic activity of other porous metal oxides of different compositions toward OER, and a related study is currently under way.

## Acknowledgements

This work was supported by IBS-R023-D1, KEIT-10047717 and BioNano Health-Guard Research Center funded by the Ministry of Science, Information and Communication Technology (ICT) and Future Planning of Korea as Global Frontier Project (Grant No. H-GUARD\_NRF 2013M3A6B2078946). We thank KBSI for allowing us to use their HRTEM and ICP-AES instruments, and also Prof. Chang Seop Hong and Dong Won Kang in Department of Chemistry of Korea University for BET measurements.

## Notes and references

- 1 A. Kudo and Y. Miseki, *Chem. Soc. Rev.*, 2009, **38**, 253.
- 2 Y. Tachibana, L. Vayssieres and J. R. Durrant, *Nat. Photonics*, 2012, **6**, 511.
- 3 T. Hisatomi, J. Kubota and K. Domen, *Chem. Soc. Rev.*, 2014, **43**, 7520.
- 4 J. Suntivich, K. J. May, H. A. Gasteiger, J. B. Goodenough and Y. Shao-Horn, *Science*, 2011, **334**, 1383.
- 5 D. Galizzioli, F. Tantardini and S. Trasatti, *J. Appl. Electrochem.*, 1974, **4**, 57.
- 6 J. Horkans and M. W. Shafer, *J. Electrochem. Soc.*, 1977, **124**, 1202.
- 7 C. Felix, T. Maiyalagan, S. Pasupathi, B. Bladergroen and V. Linkov, *Int. J. Electrochem. Sci.*, 2012, **7**, 12064.
- 8 Z. Gui, E. Gillette, J. Duay, J. Hu, N. Kim and S. B. Lee, *Phys. Chem. Chem. Phys.*, 2015, **17**, 15173.
- 9 D. M. Robinson, Y. B. Go, M. Mui, G. Gardner, Z. Zhang, D. Mastrogianni, E. Garfunkel, J. Li, M. Greenblatt and G. C. Dismukes, *J. Am. Chem. Soc.*, 2013, **135**, 3494.
- 10 J. D. Blakemore, H. B. Gray, J. R. Winkler and A. M. Muller, *ACS Catal.*, 2013, **3**, 2497.
- 11 S. C. Riha, B. M. Klahr, E. C. Tyo, S. Seifert, S. Vajda, M. J. Pellin, T. W. Hamann and A. B. F. Martinson, *ACS Nano*, 2013, **7**, 2396.
- 12 A. Ramirez, P. Hillebrand, D. Stellmach, M. M. May, P. Bogdanoff and S. Fiechter, *J. Phys. Chem. C*, 2014, **118**, 14073.
- 13 A. Singh, S. L. Y. Chang, R. K. Hocking, U. Bach and L. Spiccia, *Energy Environ. Sci.*, 2013, **6**, 579.
- 14 K. Zhang, X. Han, Z. Hu, X. Zhang, Z. Tao and J. Chen, *Chem. Soc. Rev.*, 2015, **44**, 699.
- 15 V. B. R. Boppa and F. Jiao, *Chem. Commun.*, 2011, **47**, 8973.
- 16 I. Zaharieva, M. M. Najafpour, M. Wiechen, M. Haumann, P. Kurz and H. Dau, *Energy Environ. Sci.*, 2011, **4**, 2400.
- 17 X. Duan, J. Yang, H. Gao, J. Ma, L. Jiao and W. Zheng, *CrystEngComm*, 2012, **14**, 4196.
- 18 P. Pal, S. K. Pahari, A. K. Giri, S. Pal, H. C. Bajajab and A. B. Panda, *J. Mater. Chem. A*, 2013, **1**, 10251.
- 19 Y. S. Hu, A. Kleiman-Shwarscstein, A. J. Forman, D. Hazen, J. N. Park and E. W. McFarland, *Chem. Mater.*, 2008, **20**, 3803.
- 20 X. Zhang, H. Li, S. Wang, F. R. F. Fan and A. J. Bard, *J. Phys. Chem. C*, 2014, **118**, 16842.
- 21 T. Grewe, X. Deng and H. Tüysüz, *Chem. Mater.*, 2014, **26**, 3162.
- 22 R. Frydendal, M. Busch, N. B. Halck, E. A. Paoli, P. Krtil, I. Chorkendorff and J. Rossmeisl, *ChemCatChem*, 2015, **7**, 149.
- 23 Y. Gorlin, C. J. Chung, J. D. Benck, D. Nordlund, L. Seitz, T. C. Weng, D. Sokaras, B. M. Clemens and T. F. Jaramillo, *J. Am. Chem. Soc.*, 2014, **136**, 4920.
- 24 C. H. Kuo, W. Li, L. Pahalagedara, A. M. El-Sawy, D. Kriz, N. Genz, C. Guild, T. Ressler, S. L. Suib and J. He, *Angew. Chem., Int. Ed.*, 2015, **54**, 2345.
- 25 A. Bergmann, I. Zaharieva, H. Dau and P. Strasser, *Energy Environ. Sci.*, 2013, **6**, 2745.
- 26 J. Kang, A. Hirata, L. Kang, X. Zhang, Y. Hou, L. Chen, C. Li, T. Fujita, K. Akagi and M. Chen, *Angew. Chem., Int. Ed.*, 2013, **52**, 1664.
- 27 Y. Meng, W. Song, H. Huang, Z. Ren, S. Y. Chen and S. L. Suib, *J. Am. Chem. Soc.*, 2014, **136**, 11452.
- 28 M. Fekete, R. K. Hocking, S. L. Y. Chang, C. Italiano, A. F. Patti, F. Arena and L. Spiccia, *Energy Environ. Sci.*, 2013, **6**, 2222.
- 29 M. Risch, V. Khare, I. Zaharieva, L. Gerencser, P. Chernev and H. Dau, *J. Am. Chem. Soc.*, 2009, **131**, 6936.
- 30 M. Risch, K. Klingan, J. Heidkamp, D. Ehrenberg, P. Chernev, I. Zaharieva and H. Dau, *Chem. Commun.*, 2011, **47**, 11912.
- 31 J. B. Gerken, J. G. McAlpin, J. Y. C. Chen, M. L. Rigsby, W. H. Casey, R. D. Britt and S. S. Stahl, *J. Am. Chem. Soc.*, 2011, **133**, 14431.
- 32 T. A. Mellan, K. P. Maenetja, P. E. Ngoepe, S. M. Woodley, C. R. A. Catlow and R. Grau-Crespo, *J. Mater. Chem. A*, 2013, **1**, 14879.
- 33 P. Ruetschi and R. Giovanoli, *J. Electrochem. Soc.*, 1988, **135**, 2663.
- 34 A. Iyer, J. Del-Pilar, C. K. King'ondou, E. Kissel, H. F. Garces, H. Huang, A. M. El-Sawy, P. K. Dutta and S. L. Suib, *J. Phys. Chem. C*, 2012, **116**, 6474.
- 35 F. Cheng, T. Zhang, Y. Zhang, J. Du, X. Han and J. Chen, *Angew. Chem., Int. Ed.*, 2013, **52**, 2474.